Compatibilizing Polyimide/Silica Hybrids by Alkoxisilane-Terminated Oligoimides: Morphology–Properties Relationships

Giuseppe Ragosta, Pellegrino Musto, Mario Abbate, Gennaro Scarinzi

Institute of Chemistry and Technology of Polymers, National Research Council of Italy, via Campi Flegrei, 34, Pozzuoli (NA) 80078, Italy

ABSTRACT: A fluorinated polyimide (PI), synthesized from 4,4′-(hexafluoroisopropylidene) diphthalic anhydride and 4,4′-diaminodiphenyl ether, was used as matrix for the preparation of PI/silica hybrids. The inorganic phase was obtained *in situ* by a sol–gel route with tetraethoxysilane as precursor. Both micron- and nano-scale hybrids were obtained depending on the interfacial interaction between the organic and inorganic phases. To promote such interaction a compatibilizing agent was synthesized, in the form of an alkoxisilane-terminated oligoimide. Both the PI and the coupling agent were characterized by FTIR and Raman spectroscopies and by GPC measurements. The effect of the coupling agent on the morphology of the hybrids and on the size of the silica particles was investigated by scanning electron microscopy. The viscoelastic, mechanical, and thermal properties of hybrid composites were studied. It was shown that by adding appropriate amounts of the compatibilizer it was possible to control the morphology and to obtain homogeneous nanostructured systems. A general improvement of the mechanical performances and of the thermal stability was demonstrated, together with an increase of T_g, which was found more pronounced for the nanocomposites than for the microcomposites. © 2011 Wiley Periodicals, Inc. J Appl Polym Sci 121: 2168–2186, 2011

Key words: nanocomposites; polyimide; morphology; mechanical properties; thermal stability

INTRODUCTION

Among aromatic polymers, polyimides (PIs) exhibit outstanding characteristics such as high tensile strength and modulus, high thermal stability and solvent resistance, coupled with relatively low permittivity, and dielectric losses up to very high temperatures. For this reason, they find applications in aerospace, microelectronic devices, and in separation membrane technology and are well-known as important high performance polymers.[1–5] Thermal and mechanical properties of PIs can be further improved by inclusion of silica in the matrix to produce organic–inorganic hybrid materials.[6–10] The sol–gel process represents the main route to develop silica particles *in situ* in the PI matrix.[11–13] The morphology of the resulting hybrids can assume either nanostructural or microstructural features, depending on the reaction conditions and on the degree of compatibility between the organic and inorganic components. In earlier studies only hybrids with large silica domains scarcely bonded to the PI matrix were produced. This led to brittle materials with poor mechanical properties. Later on, to enhance the compatibility between the silica phase and the PI matrix, a variety of organosilanes as coupling agents have been used. The role of these molecules is to provide, through their functionalities, a connection between the inorganic silica network and the organic polymer.[14–18]

In previous studies,[19–24] we have found that the morphology of PI/silica hybrids can be closely controlled by using a (γ-glycidyloxypropyl)trimethoxylane (GOTMS) as coupling agent. Discontinuous, two-phase microcomposites were obtained in absence of GOTMS, whereas bicontinuous nanocomposites were achieved by introducing the GOTMS in the precursor solution for the formation of the silica network. The way through which the coupling agent determined the evolution of the morphology in these hybrid systems was attributed to interactions by hydrogen bonding taking place between the epoxy groups of GOTMS and the acid groups of the PI precursor. Attempts to improve the compatibility in PI/silica hybrids were also made by Wang *et al.*[14,25,26] by using an aminophenyl-trimethoxysilane as coupling agent. Although premixed with the PI precursor or with the tetramethoxysilane solution, this coupling agent was reported to improve the dispersion of the silica domains in the PI matrix. This was

Correspondence to: G. Ragosta (rago@ictp.cnr.it).
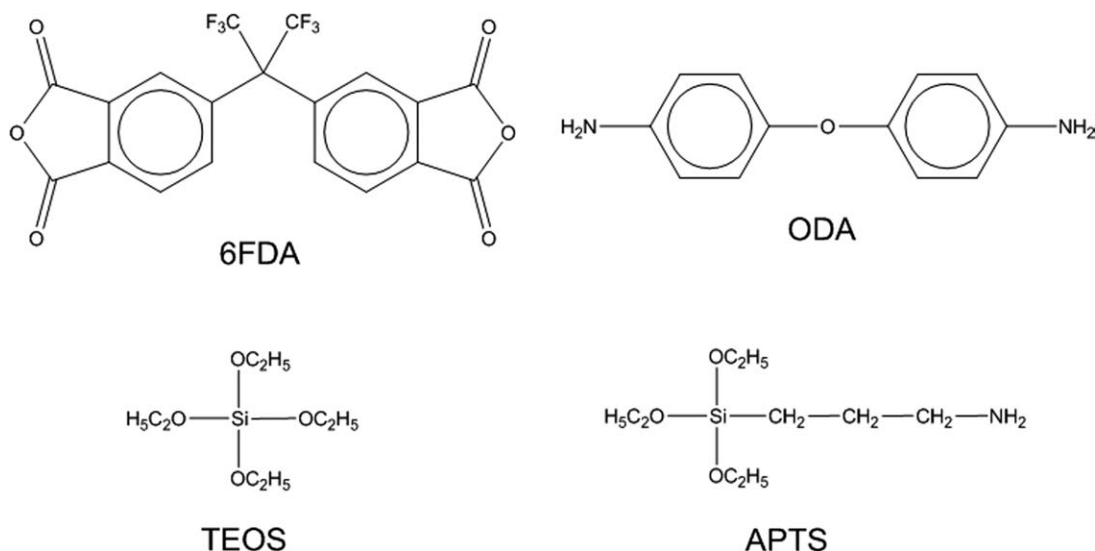
Scheme 1 Chemical formulas of the materials used in the preparation of the hybrids

attributed to the enhanced interconnectivity of the two phases through chemical interactions with the amine groups of the coupling agent. Numerous other studies[27,28] have proved that different coupling agents had pronounced effects on the morphology of the PI/silica hybrids and improved the mechanical strength and the thermal stability.

Surface modification of the inorganic particles has been also considered to be a suitable approach for tailoring sol–gel materials to make them compatible with the PI matrix through improved interfacial interaction.[18,29] Similarly, the modification of the matrix itself in a way to create reactive sites toward the inorganic network has also been demonstrated to be an alternative method to the particle's surface modification or to the addition of coupling agents.[28,30]

As PI-silica hybrids combine the basic properties of organic and inorganic constituents, they can also offer specific advantages for the preparation of membranes with enhanced selectivity and permeability.[31,32] In particular, PI/silica hybrids, based on fluorinated PIs, have been found to exhibit promising gas permeation characteristics and have been tailored to accomplish specific gas separations. Cornelius et al.[33] prepared a series of hybrid composites using fluorinated PIs and various organosilica structures. They found that the gas transport properties were dependent on the type of alkoxide used and on the final morphology. In particular, systems with a low compatibility showed low membrane performances. In contrast, improvements in selectivity and permeability were observed in hybrids with high interactions between the components.

Fluorinated PIs are also representative of a growing class of materials that for space and electronic applications have several desirable properties such as solubility in a variety of solvents, low moisture sorption, enhanced processability, and optical transparency while maintaining the thermal-oxidative stability associated with traditional PIs. However, they often have elevated linear coefficients of thermal expansion (CTE), which limit their use in space applications. The incorporation of a silica phase within fluorinated PIs have been found to be very effective in modulating the linear CTE.[34,35]

The aim of the present study is to enhance the mechanical properties and the thermo-oxidative stability of fluorinated PIs used as gas separation membranes and for space and electronic applications, by formulating hybrid materials with controlled morphology. The inorganic phase (silica) was produced in situ via a sol–gel process, and the morphology control was achieved by a suitably synthesized coupling agent, consisting of an alkoxisilane terminated oligoimide.

The synthesis of both PI and coupling agent was followed by FTIR and Raman spectroscopies and by GPC measurements. The effect of the coupling agent on the morphology of the prepared hybrids and on the size of silica particles was investigated by scanning electron microscopy. The viscoelastic, mechanical, and thermal properties of hybrid composites developed with and without the coupling agent were compared and correlated to their molecular structure. Furthermore, analytical methods were used to obtain kinetic parameters of the thermal degradation process.

EXPERIMENTAL

Materials

The molecular structures of the monomers used in the hybrids synthesis are reported in Scheme 1. All the reagents and solvents were purchased from Sigma-Aldrich. 4,4′-(Hexafluoroisopropylidene)

TABLE I
Composition of Microcomposite and Nanocomposite Hybrids

Silica content (wt %)	Microcomposites		Nanocomposites		
	HMW polyimide (g)	TEOS (g)	HMW polyimide (g)	APTS end-capped oligoimide (g)	TEOS (g)
5	0.284	0.078	0.250	0.250	0.138
10	0.286	0.163	0.250	0.250	0.300
15	0.284	0.262	0.250	0.250	0.462
20	0.286	0.374	0.250	0.250	0.654

diphthalic anhydride (6FDA) and 4,4′-diaminodiphenyl ether (ODA) were purified by vacuum sublimation and stored under vacuum. Tetraethoxysilane (TEOS), (3-aminopropyl)triethoxysilane (APTS), and dichloromethane (DCM) were used as received. N-Methyl-2-pyrrolidone (NMP) was stirred over night on phosphorus pentoxide, distilled under vacuum, and stored under nitrogen.

Synthesis of the high-molecular weight polyamic acid

In a 50–mL, three-necked, round-bottomed flask equipped with a nitrogen inlet, a magnetic stirrer, and a dropping funnel 0.905 g (4.523 mmol) of ODA was dissolved in 8.1 mL of NMP. In a 25–mL, two–necked, round-bottomed flask 2.008 g (4.523 mmol) of 6FDA was dissolved, under nitrogen, in 7.0 mL of NMP. With the aid of the dropping funnel, the 6FDA solution was slowly added to the ODA solution with vigorous stirring under nitrogen purge. The dropping funnel was rinsed three times with 1-mL NMP. After 24-h mixing at RT, a viscous polyamic acid solution was obtained. The product was stored at −18°C.

Synthesis of the anhydride-terminated amic acid oligomer

The anhydride-terminated amic acid oligomer was prepared following the same synthetic scheme described for the high molecular weight polymer. An excess of the 6FDA monomer was added to ensure the anhydride end-capping of the chains. A mol ratio of ODA/6FDA of 0.90 was used. The polyamic acid solution was stored at −18°C.

PI film preparation

The polyamic acids were thermally cyclised to PIs by casting 3.0 mL of the solution on a glass plate using a Gardner knife. The applicator was adjusted to obtain 30-μm thick films after curing. The films were evaporated for 1 h at 80°C and cured stepwise at 100, 150, 200, 250, and 290°C for 1 h at each temperature. The high-molecular weight PI films were detached from the glass plate by immersion in water at RT. The PI oligomer cracked on cooling of the

plate to RT and spontaneously detached from the substrate. The densities of the PI and of the silica phase, as determined by hydrostatic balance at 20°C, were 1.409 and 1.974 g cm^{-3} respectively.

Preparation of the silica precursor

The silica precursor was prepared as a prehydrolyzed TEOS solution as reported elsewhere.[19]

PI/silica microcomposite preparation

In the following, it is reported the preparation of a representative microcomposite (10% wt of silica). High-molecular weight PI (0.286 g) along with 3.0 mL of NMP was charged in a two-necked, round-bottomed, glass flask equipped with a magnetic stirring bar and a nitrogen inlet. The flask was heated to 110°C up to complete dissolution of the polymer. At RT, in air, under vigorous stirring 0.163 g of prehydrolyzed silica precursor was added drop wise. After 10 min of intense stirring, a clear solution was obtained. Films of the microcomposite were casted and cured following the same procedure described for the plain PI. Opaque films were produced. The compositions of all investigated systems are reported in Table I.

APTS end-capping of the anhydride-terminated imide oligomer

A total of 0.300 g of the anhydride-terminated imide oligomer (0.048 mmol of anhydride groups) was placed in a two-necked, round-bottomed, 25-mL, glass flask and dried under vacuum at 120°C for 6 h. The temperature was lowered to RT and, under nitrogen atmosphere, 2.7 mL of NMP was added. The flask was heated at 60°C to allow the complete dissolution of the oligomer. At RT, under vigorous magnetic stirring, 24.5 μL (0.105 mmol) of APTS was added by means of a micropipette. The end-capping reaction was carried out at RT for 1 h under nitrogen purge.

Raman analysis of the end-capping reaction

In the following, the experiment relative to a 2/1 APTS/anhydride molar ratio is reported. One

hundred and fifty six milligrams (0.026 mmol anhydride groups) of oligoimide was dried at 120°C, under vacuum for 5 h. At RT, under inert atmosphere, the oligomer was dissolved in 0.6 mL (0.80 g) of DCM. On complete dissolution, 12.6 µL (0.060 mmol) of APTS were added by means of a micropipette. The system was kept under stirring for 5 min. Samples of the reaction solution were periodically withdrawn and analyzed by means Raman spectroscopy.

PI/silica nanocomposite preparation

In the following, is reported the preparation of a representative nanocomposite (10% wt of silica). In a two-necked round-bottomed flask, equipped with a magnetic stirrer and a nitrogen gas inlet 0.250 g of high molecular weight PI was dissolved, at 110°C, in 2.2 mL of NMP. The temperature was lowered to RT and, under vigorous stirring, 2.50 g of the APTS end-capped oligoimide solution was added. After 20 min of mixing, 0.30 g of the prehydrolyzed silica precursor was added dropwise under vigorous stirring. The mixture was stirred at room temperature for 1 h 30 min. A clear and homogeneous system was obtained. The nanocomposite precursor was casted on a glass plate and cured following the same procedure described for the plain PI. Transparent films were produced. Similar procedures were adopted for 15 and 20 wt % compositions and also in these cases transparent and visually homogeneous films were obtained.

Techniques

Viscosity measurements

Viscosities of PIs were measured at 30°C at a concentration of 0.5 dL/g in NMP, using an Ubbelohde viscosimeter.

GPC measurements

GPC measurements were performed by a Waters ISO C instrument equipped with an Evaporative Light Scattering PL-ELS 2100 detector and a Poly-Pore 7.5 mm ID column. The measurements were carried out at 30°C using THF as an eluent at a flow rate of 1 mL/min. The concentration of the samples was 0.5 mg/mL.

FTIR spectroscopy

FTIR transmission spectra were collected by a System-2000 spectrometer from Perkin-Elmer (Norwalk, CT), equipped with a Germanium/KBr beam splitter and a wide-band DTGS detector. The instrumental parameters for data collection were as follows: resolution $= 4$ cm^{-1}, optical path difference velocity $= 0.2$ cm/s, spectral range $= 4000$–400 cm^{-1}. A total of 16–32 data collections were averaged for each spectrum to improve the signal-to-noise ratio (SNR).

FT-Raman

FT-Raman spectra were collected with a Nexus-670 FT-Raman spectrometer from Nicolet (Madison, WI), equipped with a CaF$_2$ beam splitter and an Indium-Gallium Arsenide (InGaAs) photoelectric detector. The radiation was collected with a 180° backscattering geometry. The excitation source was a diode-pumped Nd-YO$_4$ laser emitting in the Near Infrared at $\lambda = 1064$ nm, which operates at a laser power of 750 mW. The spectra were collected in a Raman-shift range between 100 and 3700 cm^{-1} at a resolution of 4 cm^{-1}. Signal averaging over at least 1000 data collections was performed to improve the SNR.

Dynamic mechanical tests

Dynamic-mechanical tests were carried out using a Perkin–Elmer Pyris Diamond DMA apparatus. The measurements were performed in tensile mode at frequencies of 0.05, 0.1, 0.2, 0.5, 1, 2, 5, 10, and 20 Hz at a constant heating rate of 3°C/min and in the temperature range from −150 to 450°C. Samples 50-mm long, 10-mm wide, and 40-µm thick were used. The storage modulus (E'), loss modulus (E'') and loss tangent (tan δ) were recorded.

Tensile mechanical tests

Stress–strain analysis was carried out under ASTM 882 that covers the measurements of tensile properties of plastics in the form of thin films. Dumb-bell specimens having a constant width of 3.5 mm in the gauge length region were used. The samples were tested using a universal testing machine (Instron mod. 4505) at uniform strain rate of 1 mm/min and at ambient temperature. From the stress–strain curves modulus, ultimate tensile strength and strain at break were calculated. The average value obtained from tensile measurements using four to five samples was reported in each case.

Morphology

The morphology of the hybrid films was studied using a Quanta 200 FEI scanning electron microscope (FEI-SEM). The samples were quenched in liquid nitrogen and brittle fractured. These were mounted on aluminium holder specially designed for thin films, vacuum dried and sputter-coated with a thin layer of chromium, before examination.
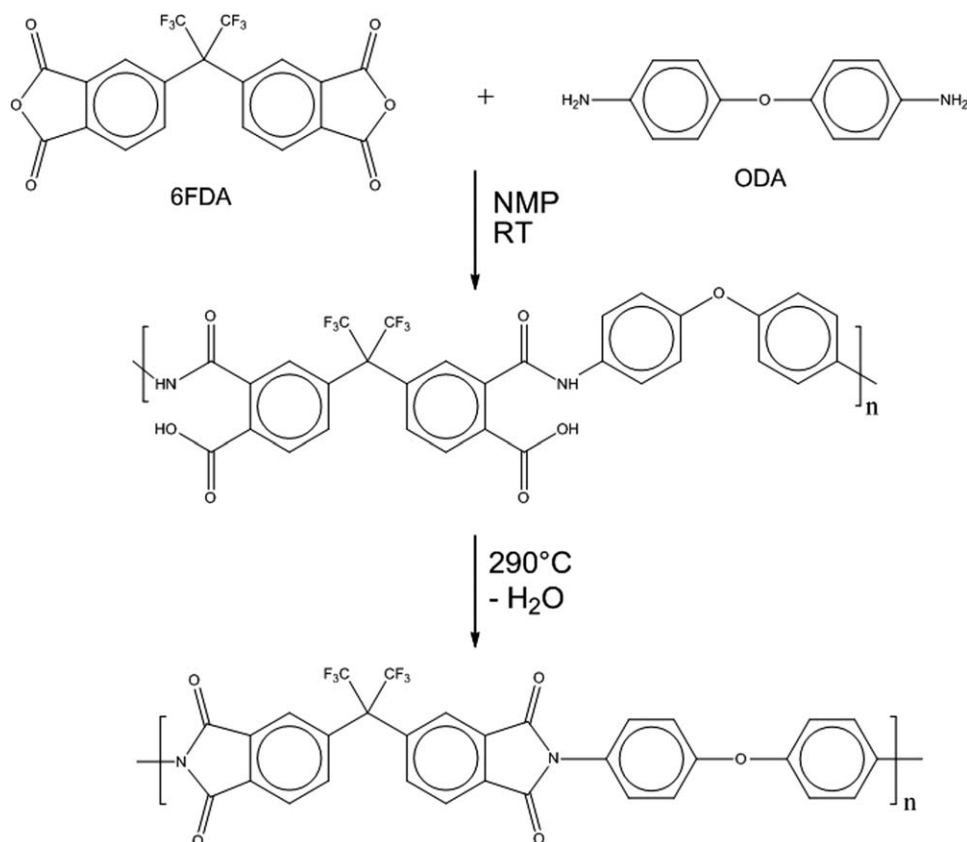
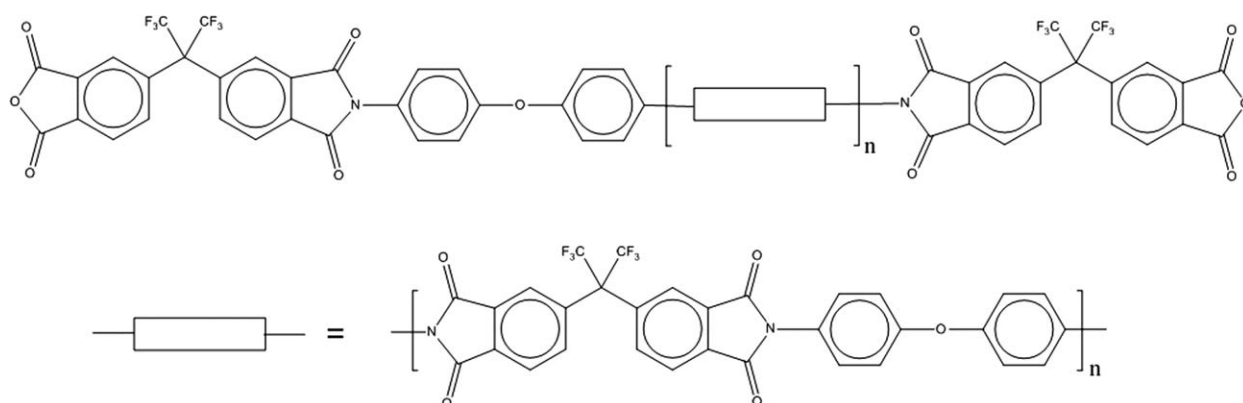**Scheme 2**   Synthesis of the high molecular weight PI

Thermogravimetric analysis

The thermal degradation of the hybrid systems was investigated by a thermogravimetric analyzer (Perkin-Elmer Pyris Diamond TG/DTA) from ambient temperature to 800°C with various heating rates (i.e., 2, 5, 10, 20, and 40°C/min) under air atmosphere. The measurements were conducted using 6–10 mg samples. Weight-loss/temperature curves were recorded.

RESULTS AND DISCUSSION

Synthesis of the PI and the hybrids

The high-molecular weight 6FDA-ODA PI was synthesized following a two-step procedure reported in the literature.[36] As shown in Scheme 2, in the first step, a polyamic acid (AMA) solution was prepared by reacting equimolecular amounts of the diamine and the dianhydride monomers, at room temperature, in NMP. In

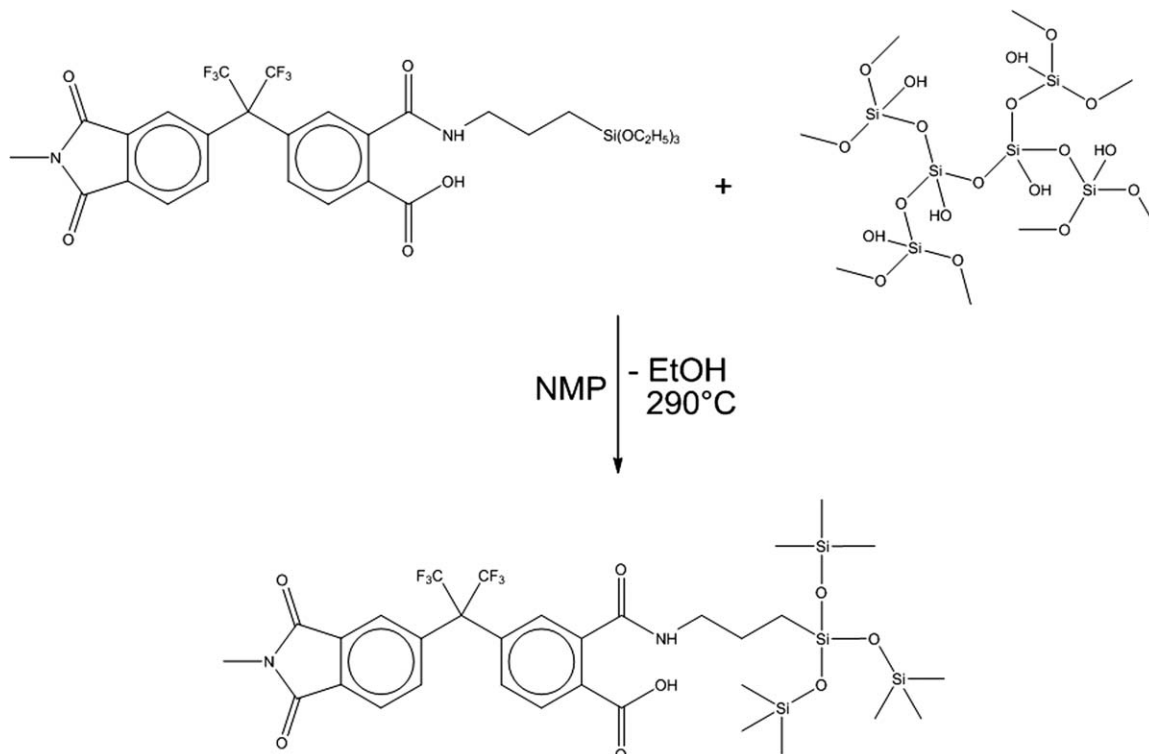**Scheme 3**   Structure of the low molecular weight anhydride terminated oligoimide
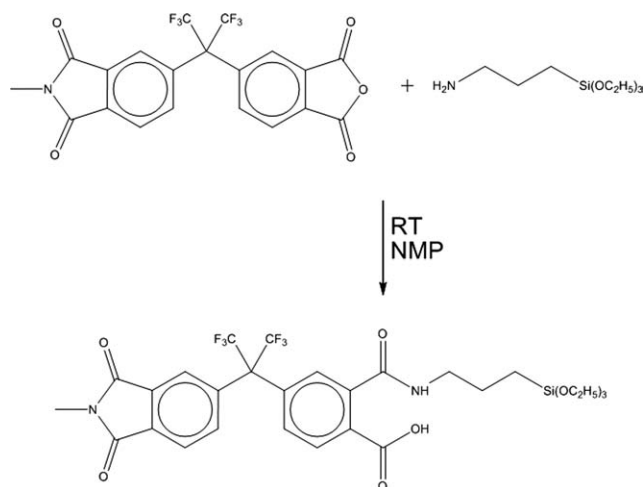
Scheme 4 Synthesis of the alkoxisilane terminated oligoimide

the second step, the AMA solution was evaporated and thermally cyclized on a glass substrate.

The structure of the low molecular weight, anhydride terminated oligoimide is reported in Scheme 3. It was obtained following the same two-step procedure described for the high-molecular weight polymer.

To produce the desired anhydride terminals an excess of 6FDA was used. The molar ratio between the amine and anhydride monomer was 0.90. According to the Carothers equation for step-growth polymerization,[37] this reactants ratio would produce

a degree of polymerization of 19 and a $\overline{M}_n$ of 1.15×10^4 g/mol.

To produce hybrids with micrometric particles (microcomposites) a high-molecular weight PI, dissolved in NMP, was mixed with the prehydrolyzed silica precursor. The resulting clear solution was evaporated and cured. Opaque films were obtained, which indicates the presence of a microphase separation between the hybrid components.

The nanohybrid samples were prepared following the same scheme described for the microcomposites but the additional use of an alkoxisilane terminated oligoimide. The end-capping reaction of the PI is reported in Scheme 4. The NMP solution obtained is directly used in the synthesis of the nanohybrid.

The end-capped oligoimide is mixed with the high-molecular weight PI solution and the prehydrolyzed silica precursor. As shown in Scheme 5, during the evaporation and curing of the cast films, the alkoxisilane terminal groups of the modified oligomer are involved in the condensation reaction of the silica precursor. In this way, the silica phase results to be covalently linked to the organic component of the nanohybrid.

Spectroscopic characterization

The transmission FTIR spectrum of the high-molecular weight PI in the form of a thin film [(3.0 ± 1.0) µm] is reported in Figure 1. Peaks characteristic of

Scheme 5 Reaction between the alkoxisilane terminated oligoimide and the silica precursor for the preparation of the nanohybrids
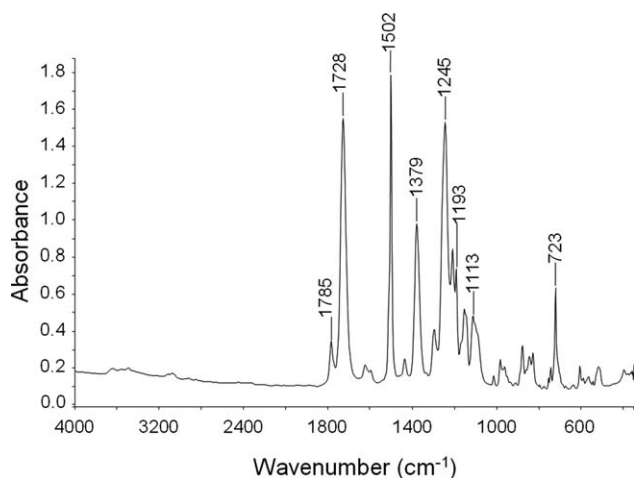
Figure 1 FTIR spectrum in the wavenumber range 4000–400 cm^{-1} of the high-molecular weight polyimide.

the imide ring are identified at 1785 cm^{-1} [$v_{ip}(C=O)$], 1728 cm^{-1} [$v_{op}(C=O)$], 1379 cm^{-1} [$v(C-N)(O-C)_2(N-C)$], 1113 cm^{-1} [$(O-C)_2(N-C)$, imide III band] and at 723 cm^{-1} [in-plane imide ring deformation].[38,39] In the above, the subscripts *op* and *op* stand for in-phase and out-of-phase stretching, respectively. The absence of residual absorption from amic acid groups [1690 cm^{-1}, $v(C=O)$] demonstrates the essentially complete conversion of polyamic acid into PI in the chosen imidization conditions. Other prominent peaks of the PI spectrum are observed, according to the proposed molecular structure, at 1502 cm^{-1} [phenyl $v_{sym}(C-C)$] and 1245–1193 cm^{-1} [$v(CF_3)$].[40,41] The oligoimide is very brittle and unsuitable for the preparation of a good quality, free-standing film. It is, however, soluble in DCM, which affords IR sampling in solution. The relative spectrum (concentration = 13.3 mg/mL) is reported in Figure 2(A). The 6FDA anhydride in DCM produces a fully resolved doublet at 1858 cm^{-1} [$v_{ip}(C=O)$] and 1788 cm^{-1} [$v_{op}(C=O)$] [see the inset of Fig. 2(B)]. In the case of the oligoimide, the 1788 cm^{-1} peak of the terminal anhydride groups is fully overlapped by the high-frequency carbonyl stretching of the imide occurring at 1785 cm^{-1}. However, the $v_{ip}(C=O)$ mode of the anhydride is fully isolated [see spectrum in Fig. 2(A)] and can even be used for quantitative purposes. In fact, making use of a calibration curve constructed by 6FDA/DCM standards of varying concentration [see Fig. 2(B)], it is possible to determine the number of terminal groups of the oligoimide and, hence, assuming two anhydride end-groups per chain, its $\overline{M}_n$ value. The FTIR analysis yielded an anhydride content of 0.64 mg mL^{-1}, which corresponds to a $\overline{M}_n$ value of 1.8×10^4 g mol^{-1}, slightly in excess with respect to the value predicted by the Carother's equation.

The spectroscopic characterization of the two prepared PIs was completed by FT-Raman measure-

ments. In Figure 3, trace A, is reported the Raman spectrum of the high-molecular weight 6FDA-ODA PI, showing two characteristic peaks of the phtalimide moiety at 1784 cm^{-1} [$v_{ip}(C=O)$] and 1730 cm^{-1} [$v_{op}(C=O)$]. Note the intensity inversion between the doublet components of the carbonyl stretching, with respect to the same normal modes in the infrared spectrum. Other peaks originating from vibrational modes of the imide ring are located at 1381 cm^{-1} [$v(C-N)(O-C)_2(N-C)$], 1117 cm^{-1} [$(O-C)_2(N-C)$, imide III band], and at 705 cm^{-1} [in-plane imide ring deformation].[40,41]

Trace B of Figure 3 refers to the spectrum of the oligoimide and is essentially coincident with the upper trace, apart from a well resolved peak at 1857 cm^{-1}, characteristic of the anhydride end-groups [$v_{ip}(C=O)$]. Here again, there is an intensity inversion between the two components of the $v(C=O)$
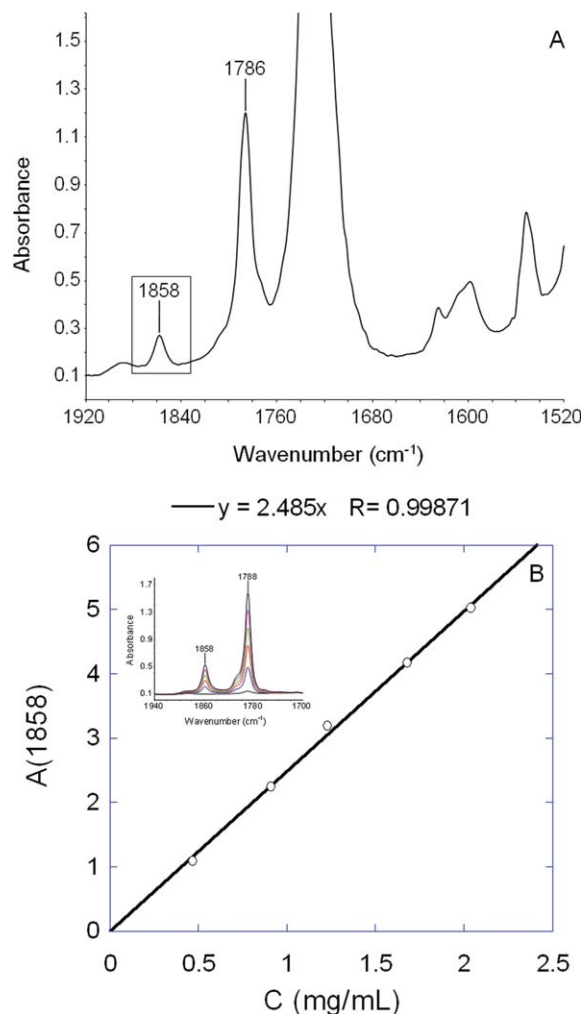

Figure 2 Quantitative analysis of end-groups by solution FTIR measurements. (A) 6FDA-ODA oligoimide in DCM (polyimide concentration = 13.3 g L^{-1}). (B) Calibration curve 6FDA-ODA anhydride in DCM. [Color figure can be viewed in the online issue, which is available at wileyonlinelibrary.com.]
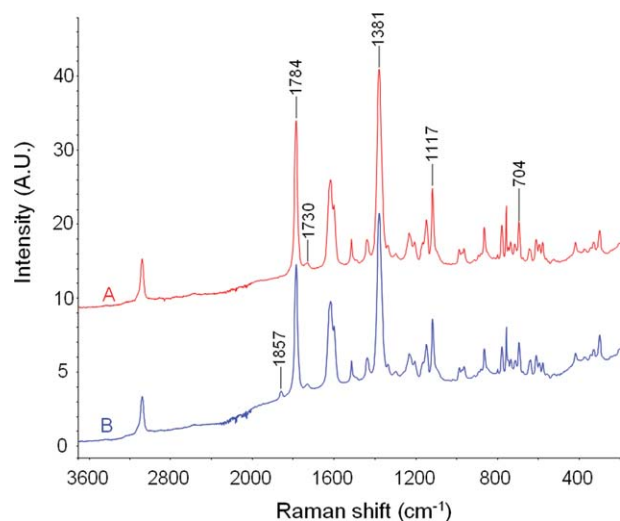
Figure 3 FT-Raman spectra of the two 6FDA-ODA samples: (A) high-molecular weight polyimide and (B) anhydride-terminated oligomer. [Color figure can be viewed in the online issue, which is available at wileyonlinelibrary.com.]

doublet in comparison to the IR spectrum, so that the in-phase mode becomes predominant in the Raman spectrum. The solubility of the oligoimide, taken together with the reduced concentration and scattering efficiency of APTS, allows one to sample directly the reactive mixture for the APTS end-capping of the oligoimide. The spectrum of the reactive mixture, before the addition of APTS, is reported in Figure 4. The inset of Figure 4 displays the anhydride carbonyl peak in different environments. In particular, trace A is the control, that is, a 16.7 wt % solution of the oligoimide in DCM (1.2×10^{-2} mol/L), traces B and C refer to the spectra collected, respectively, immediately after the addition of APTS to the control (1 : 1 molar ratio APTS/ anhydride end-groups), and after 3 h from the addition. Trace D is relative to the spectrum collected immediately after the addition of APTS in the molar ratio 2 : 1. It is found that the anhydride–APTS reaction is very fast. The Raman results indicate that, for the molar ratio 1 : 1, the conversion reaches its maximum value (75%) immediately after the reagents addition and does not increase noticeably after 3 h. Full conversion of anhydride terminals is achieved only with a twofold excess of APTS, again just after the reagent addition, a result, which allows us to adjust the stoichiometry so as to completely convert the terminal groups into alkoxisilane functionalities.

Viscometry and GPC measurements

The polyamic acids prepared from an equimolecular amount of dianhydride and diamine produced, on imidization, tough and flexible films. On the con-

trary, when an excess of dianhydride was used, on cyclization of the AMA, brittle products were obtained that cracked spontaneously. These physical features are in accordance with the viscosimetric and GPC measurements (see Fig. 5). The high-molecular weight PI prepared with an ODA/6FDA 1 : 1 molar ratio showed a $\eta_{red} = 1.5$ dL/g, $\overline{M}_n = 5.1 \times 10^4$ g/mol and $\overline{M}_w = 9.7 \times 10^4$ g/mol. Conversely, the anhydride-terminated oligoimide, prepared with an excess of 6FDA, exhibited a $\eta_{red} = 0.25$ dL/g, $\overline{M}_n = 1.4 \times 10^4$ g/mol, and $\overline{M}_w = 1.8 \times 10^4$ g/mol; the latter $\overline{M}_n$ value is in reasonable agreement with the molecular weight calculated on the basis of the FTIR analysis. Both the high-molecular weight and the oligomeric films were recovered and used for the hybrids preparation.

Morphology of the hybrid films

The FEI-SEM micrographs of the fractured surfaces of PI/silica hybrids without and with the coupling agent are reported in Fig. 6(a–d). The hybrids formed in absence of the coupling agent [Fig. 6(a,b)] show a morphology in which the inorganic phase appears in the form of ellipsoid particles with micrometric dimensions. The phase separation is the result of thermodynamic immiscibility between organic and inorganic components. The dimensions of particles for the hybrid with 7.5 vol % of silica [Fig. 6(a)] are of about 2–4 μm and 1.5 μm in the major
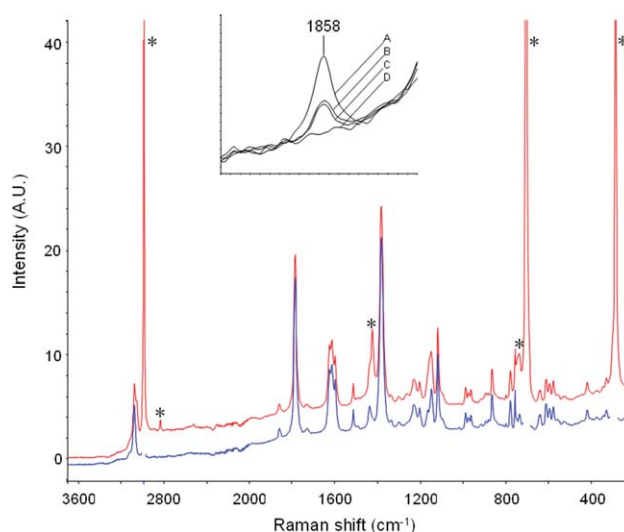

Figure 4 FT-Raman spectrum of the anhydride-terminated 6FDA-ODA as 16.7% wt/wt DCM solution. Upper trace: whole spectrum; lower trace: solvent subtracted. The inset displays the anhydride carbonyl peak in the investigated reaction mixtures. (A) control, no APTS added; (B) 1/1 amine/anhydride molar ratio immediately after APTS addition; (C) the same as B after 3 h; (D) 2/1 amine/anhydride molar ratio immediately after APTS addition. [Color figure can be viewed in the online issue, which is available at wileyonlinelibrary.com.]
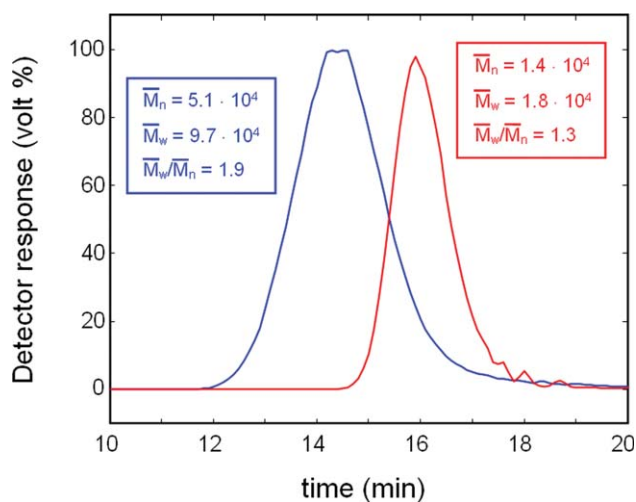
Figure 5 GPC curves of the high molecular weight polyimide (blue curve) and of the anhydride-terminated oligomer (red curve). [Color figure can be viewed in the online issue, which is available at wileyonlinelibrary.com.]

and minor axis, respectively, and increase slightly as the silica content increases [Fig. 6(b)]. These micrographs also show that the silica domains are very smooth and completely debonded from the surrounding PI matrix, indicating a very poor interfacial adhesion between the two phases. The morphology of the compatibilized hybrids is illustrated

in Fig. 6(c,d). A comparison with the hybrids of Figure 6(a,b) evidences that the coupling agent greatly reduces the dimension of the silica particles, which result spherically shaped and well bonded to the PI matrix. In fact, the surface of particles appears much rougher, indicating that a strong bond has been formed between the silica particles and the PI matrix. The particles size of the compatibilized systems is estimated to range from 50 to 80 nm, denoting the nanocomposite formation. The micrographs of Figure 6(c,d) also show the presence of few agglomerated silica domains, having a fibre-like shape. These domains are probably formed during phase separation, as the content of the silica precursor increases.

The way through which the coupling agent controls the evolution of the morphology in the compatibilized systems can be ascribed to its molecular structure that contains segments chemically identical to those of the respective phases. This allows the coupling agent to be located preferentially at the interface, favoring chemical interactions between the PI matrix and the *in situ* generated silica species. These interactions delay the onset of phase separation, resulting in a reduction of the rate of particle growth and in a better interfacial adhesion between the phases. Accordingly, a highly interconnected structure of PI chains and silica networks is produced.
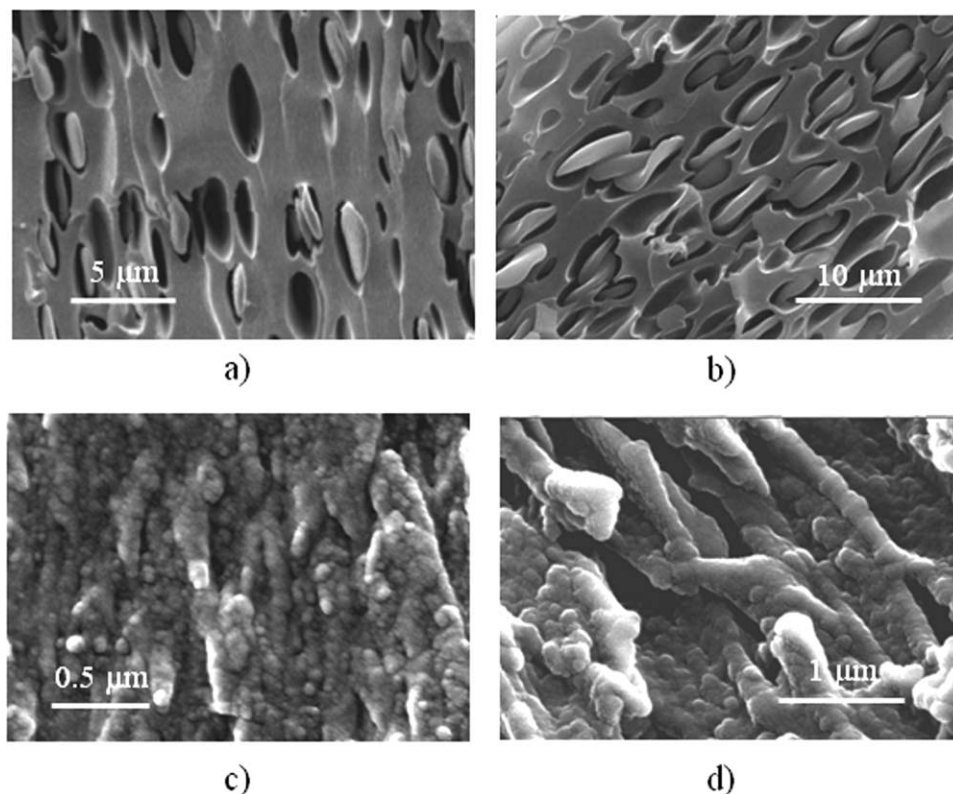

Figure 6 SEM micrographs of the cryogenically fractured surfaces of: (a) microcomposite with 7.5 vol % of silica; (b) microcomposite with 15.2 vol % of silica; (c) nanocomposite with 7.5 vol % of silica; (d) nanocomposite with 15.2 vol % of silica.
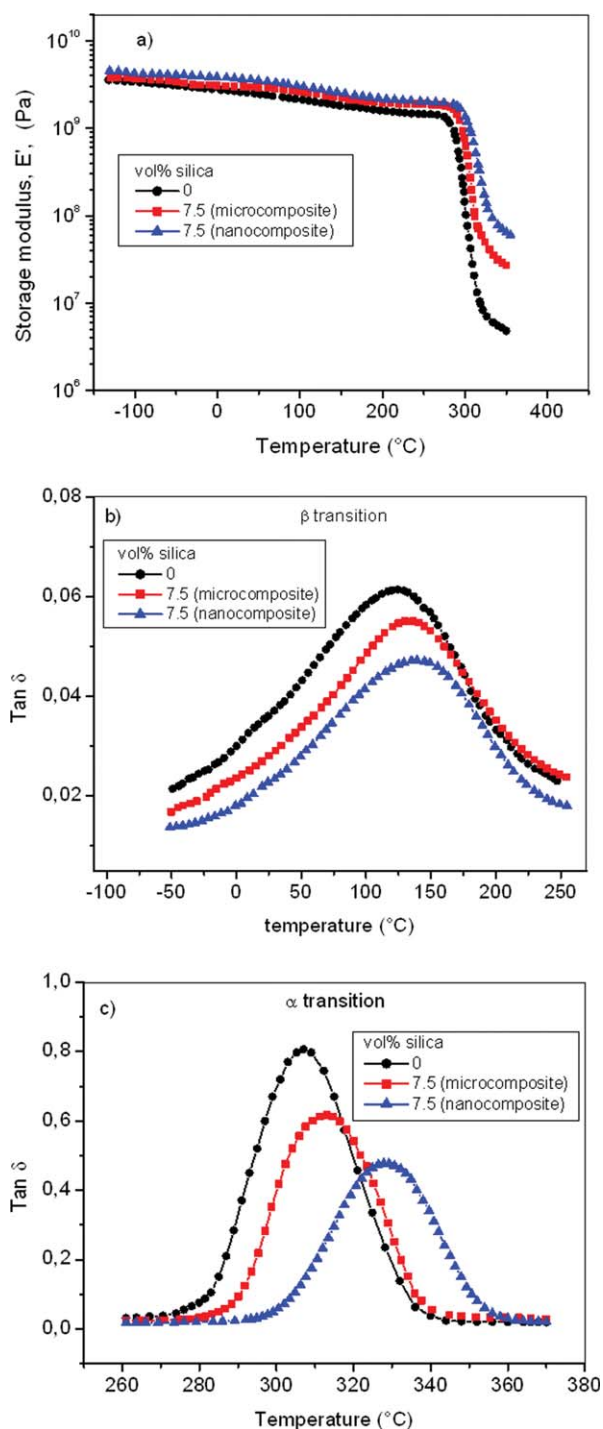
Figure 7 (a) Storage modulus (E') as a function of temperature for the pure polyimide, microcomposite with 7.5 vol % of silica and nanocomposite with 7.5 vol % of silica. (b) Loss factor (tan δ) as function of temperature in the range −50 to 250°C for the pure polyimide, microcomposite with 7.5 vol % of silica and nanocomposite with 7.5 vol % of silica. (c) Loss factor (tan δ) as function of temperature in the range 260–370°C for the pure polyimide, microcomposite with 7.5 vol % of silica and nanocomposite with 7.5 vol % of silica. [Color figure can be viewed in the online issue, which is available at wileyonlinelibrary.com.]

Viscoelastic properties

Dynamic mechanical spectra at 1 Hz, in the form of plots of storage modulus (E') and tan δ as a function of temperature, are shown in Figure 7(a–c) for the pure PI and two hybrid systems with and without the coupling agent. From the tan δ plots [Fig. 7(b,c)], two relaxations can be distinguished with increasing temperature. The relaxation taking places between −50 and 250°C is commonly referred to as the β transition, whereas the relaxation appearing at higher temperature is an α-transition process and corresponds to the glass transition temperature (T_g). In fact, in this region the storage modulus exhibits a sharp drop as shown in Figure 7(a). It is also seen from Figure 7(a) that E' is not constant at $T < T_g$ but it slightly decreases with temperature. Probably the residual stress field due to the different thermal expansion coefficients of PI and silica may induce relaxations in the polymeric matrix, which results for the negative slope of E' versus temperature.

The data of Figure 7 show that the inclusion of silica in the PI matrix produces clear changes in the dynamic-mechanical parameters. First, the storage modulus increases in both the glassy region and at temperature above the glassy transition. This enhancement is higher in the rubbery state, ensuring a better high temperature performance of the hybrid systems with respect to the pure PI. It is also apparent that the nanocomposite exhibits a rubbery modulus much higher than that displayed by the microcomposite sample. A second observation is that the presence of silica displaces the α and the β peaks toward higher temperatures. Plots of T_g and $T_β$, determined from the maxima of the tan δ curves, for all the compatibilized and noncompatibilezed systems are presented in Figures 8 and 9 as a function of silica concentration. For compatibilized hybrids, the T_g (Fig. 8) increases markedly with increasing the silica content, while for noncompatibilized materials only a slight improvement is observed. The T_g enhancement is found to be in the order of 27°C for the nanocomposite and of about 8°C for the microcomposite at a silica content of 15.2 vol %. In general, the T_g of a simple particle-filled composite rises slightly with increasing particle content. Therefore, the notable enhancement showed for nanocomposites can be ascribed to the well-bonded silica particles through the coupling agent, which restrict the segmental mobility of the PI chains involved in the α-relaxation process. Also the depression of the α-relaxation peak [see Fig. 7(c)], much larger for the nanocomposite than for the microcomposite, points to a higher constrain of the PI chains in compatibilized systems.

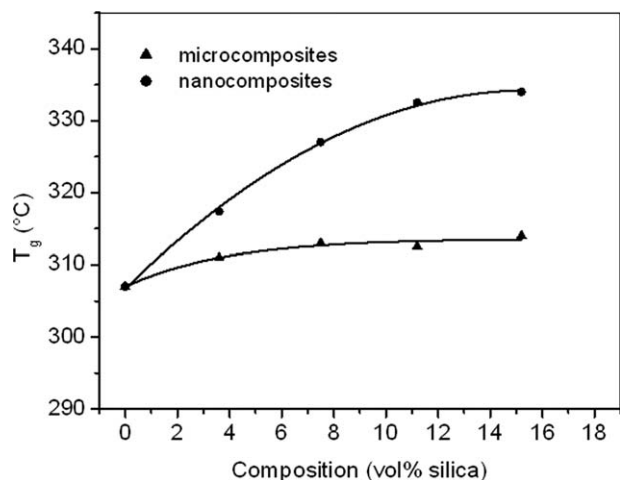As shown in Figure 9, the temperature location of the β-relaxation for compatibilized and

Figure 8 Glass transition temperature (T_g) determined from tan δ peaks as a function of the silica content for microcomposites (▲) and nanocomposites (●).

noncompatibilized hybrids increases with increasing silica content. The T_β is shifted of about 17°C for the nanocomposite and of about 7°C for the microcomposite through the addition of 15.2 vol % of silica. The β-relaxation is associated with local bond rotations and molecular segment motions along the PI backbone, and the magnitude of this relaxation is related to the concentration of segments contributing to the relaxation process. Generally, these motions are originated from diammine and/or dianhydride portions in the PI chain. As for the α-transition, the results of Figure 8 together with the reduction in the height of the β peak [Fig. 7(b)] can be ascribed to the silica domains that decrease the motions of the PI chains and the number of segments available for the β relaxation. More details on the effect of the silica morphology on the β transition were obtained by dynamic mechanical measurements performed at various frequencies.
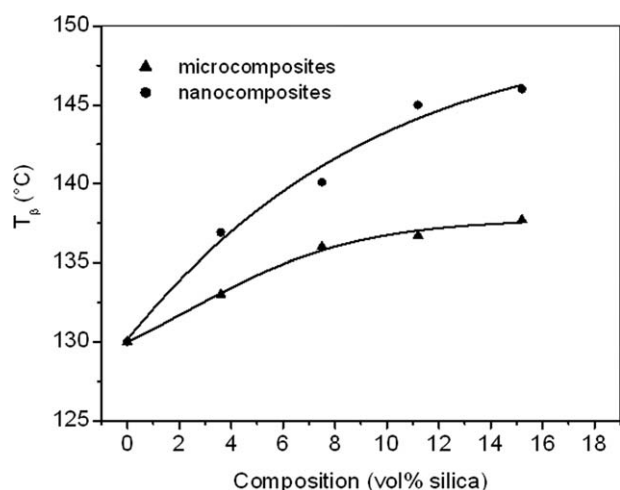
In Figure 10, for instance, the tan δ curves collected at five frequencies for a nanocomposite sample with 7.5 vol % of silica are shown. It is found that by increasing the frequency the peak maxima shift at higher temperatures while the intensities decrease. A similar trend was detected for the microcomposites and the control PI resin. This frequency dependence was examined using an Arrhenius equation, which allows to evaluate the activation energy, $E_a(\beta)$, of the β process from peak temperatures at differing frequencies.[42] The $E_a(\beta)$ values determined from the slope of Arrhenius plots (see Fig. 11) are reported in Figures 12 and 13 for microcomposite and nanocomposite systems, respectively. For the microcomposites, the activation energy increases slightly up to a silica content of 7.5 vol %, whereas at higher loadings the values are close to that of the pure PI. For the nanocomposites, instead, the activation energy increases markedly with increasing the silica concentration, confirming the higher degree of interaction between the PI chains and the silica networks through the coupling agent. This enhancement in the values of $E_a(\beta)$ is also indicative of a deviation from the localized noncooperative character of the β transition, which is characteristic of subglass polymer relaxations in general. Additional insight into the nature of the β transition was gained by the approach described by Starkweather[43] wherein the activation energy associated with secondary relaxations is related to the relaxation temperature (T') and its corresponding activation entropy (ΔS^+) at a frequency of 1 Hz:

$$E_a(\beta) = RT'[1 + \ln(k_B/2\pi h) + \ln T'] + T'\Delta S^+ \quad (1)$$

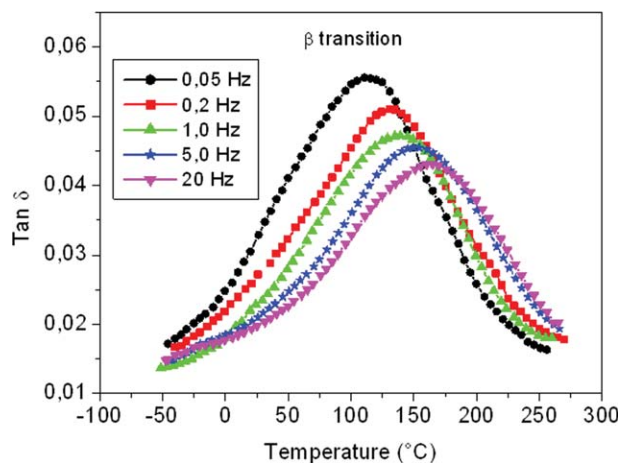where k_B and h are the Boltzmann and Planck constants, respectively. For simply non cooperative

Figure 9 Temperature of the β transition determined from tan δ peaks as a function of the silica content for microcomposites (▲) and nanocomposites (●).

Figure 10 Tan δ spectra as a function of temperature in the range −50 to 250°C for the nanocomposite hybrid containing 7.5 vol % of silica, at different frequencies. [Color figure can be viewed in the online issue, which is available at wileyonlinelibrary.com.]
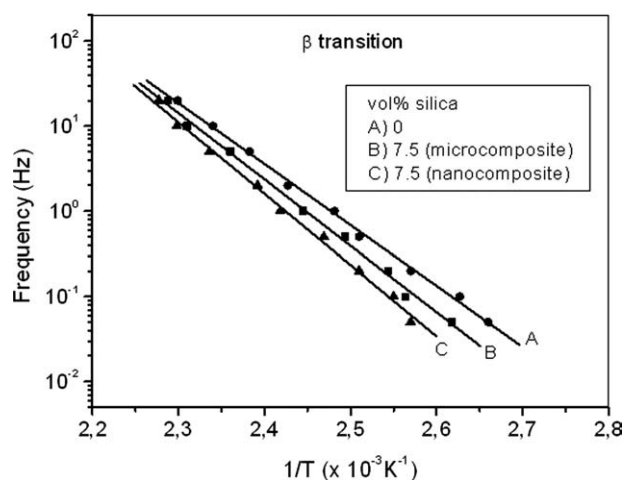
Figure 11 Arrhenius plot relative to the β transition for the pure polyimide, the nanocomposite with 7.5 vol % of silica and the microcomposite with 7.5 vol % of silica.

relaxations, Starkweather suggests that $\Delta S^+ \to 0$, with the resulting equation providing a limiting relationship between activation energy and relaxation temperature for isolated, noninteractive motional processes:

$$E_a(\beta) = RT'[1 + \ln(k_B/2\pi h) + \ln T'] \qquad (2)$$

The values of the activation energy evaluated from eq. 2 together with those of the activation entropy are shown in Figures 12 and 13. It is apparent that for the neat resin the activation energy differs from that calculated experimentally, and the value of ΔS^+ is higher than zero. These results indicate that the β transition is not completely localized but retains a limited cooperative nature. It must be underlined, however, that, according to Starkweather, ΔS^+ values up to 100 J mol^{-1} K^{-1} are still to be considered characteristic of noncooperative

motions. For nanocomposites (Fig. 12), the addition of silica progressively increase the activation entropy making the β-transition more and more cooperative in nature. This high level of cooperativity can be ascribed, again, to the interconnected silica domains that allow the PI chain segments to move in concert through the β transition. Conversely, for the microcomposite samples (Fig. 13) the existence of poor interconnected silica particles, allows only a limited degree of cooperative character, as demonstrated by the small increase in the activation entropy.

Mechanical properties

Typical tensile stress–strain curves for the pure PI and for compatibilized and noncompatibilezed hybrids containing 7.5 vol % of silica are illustrated in Figure 14. The behavior exhibited for all the samples is that of a relatively brittle material. The properties derived from the stress–strain diagrams are presented in Figures 15–17. The modulus (Fig. 15) for both microcomposites and nanocomposites increases linearly with increasing the silica content. This reinforcing effect is expected because the modulus of the silica phase, $E = 70$ GPa, is much greater than that of the PI matrix. However, the reinforcement is greater for nanocomposites than for microcomposites, presumably due to both the increased interfacial strength and the reduction in sizes of the silica particles.

Figures 16 and 17 show, respectively, the influence of the silica concentration on the tensile strength and the elongation at break. For nanocomposite hybrids, the tensile strength (Fig. 16) shows a gradual increase up to a concentration of silica around 7.5 vol %, followed by a small decrease at higher concentrations. The tensile strength is increased by
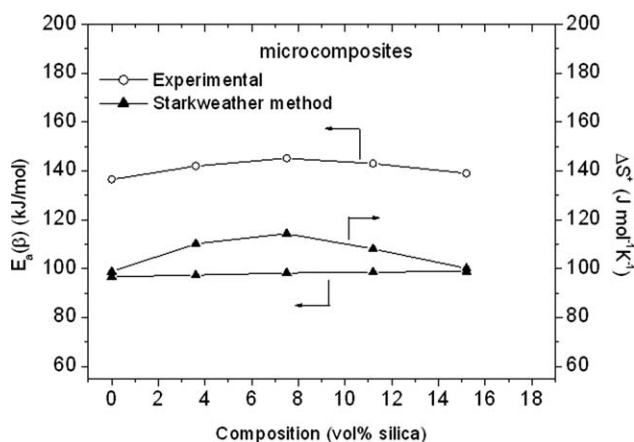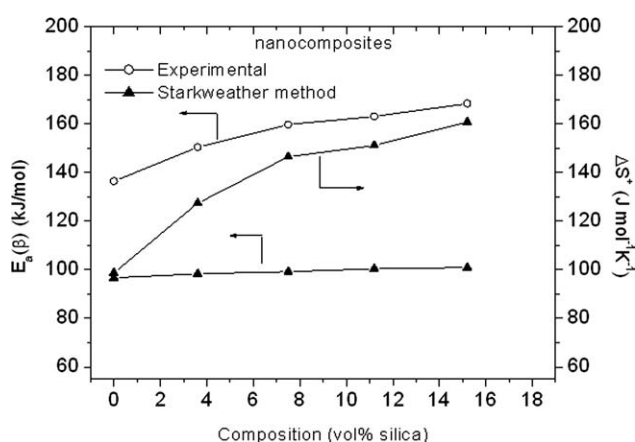

Figure 12 Activation energy, $E_a(\beta)$, and activation entropy, ΔS^+, of the β transition for the nanocomposites as a function of the silica content. (O) experimental data; (▲) data from Starkwether.

Figure 13 Activation energy, $E_a(\beta)$, and activation entropy, ΔS^+, of the β transition for the microcomposites as a function of the silica content. (O) experimental data; (▲) data from Starkwether.
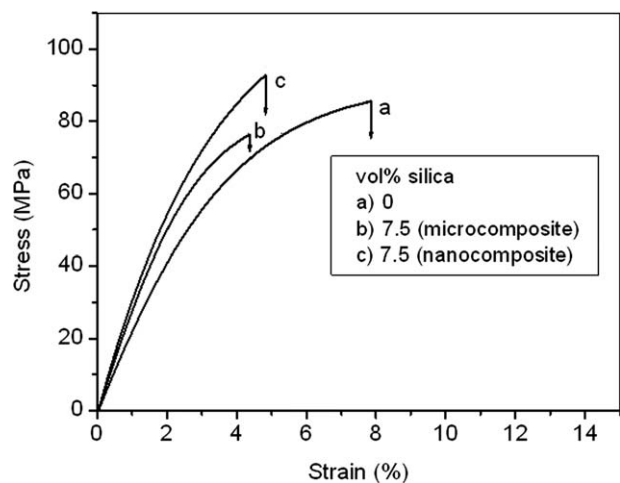
Figure 14 Typical tensile stress–strain curves of polyimide/silica hybrids: (a) pure polyimide; (b) microcomposite with 7.5 vol % of silica; (c) nanocomposite with 7.5 vol % of silica.

about 15% when 7.5 vol % of silica is introduced. On the other hand, the elongation at break, displayed in the same figure, shows a monotonic decrease. For the microcomposites (Fig. 17) one observe that the tensile strength decreases gradually over the whole composition range, whereas the elongation at break shows a behaviour very close to that of the nanocomposite samples. These results are consistent with the fact that tensile strengths for composite polymers are known to be reduced if there are no interactions between the organic matrix and the inorganic phase. In fact, the reduction in the tensile strength exhibited by the microcomposite hybrids is the result of the nonbonded silica particles that can act as stress-concentration defects, rather than as effective reinforcing fillers. However, for
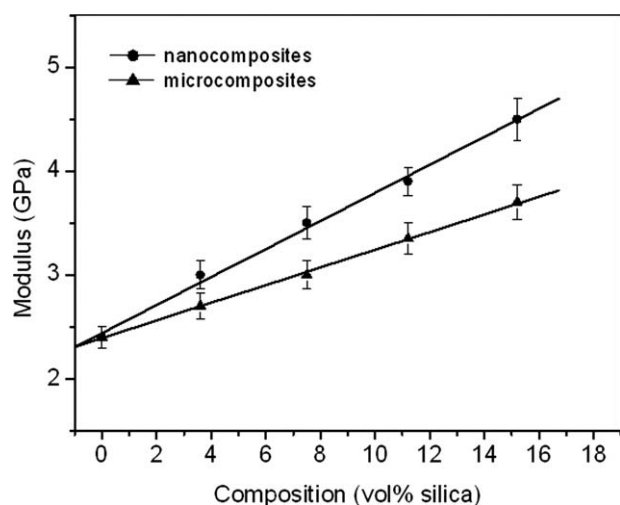

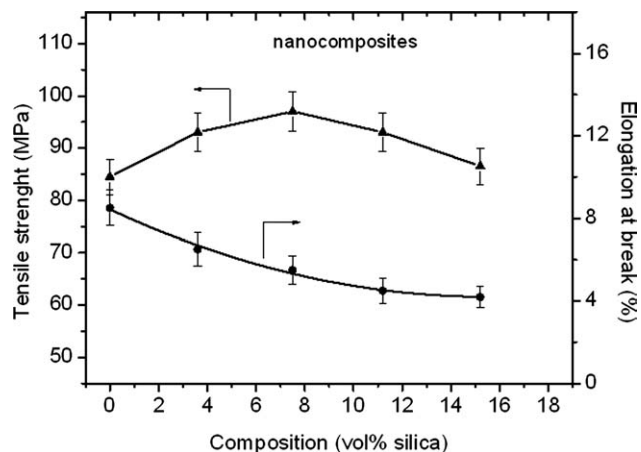**Figure 16** Tensile strength (▲) and elongation at break (●) for the nanocomposite systems as a function of the silica content.

nanocomposite in spite of the enhanced adhesion the elongation at break slightly decreases. This can be related to the inherently low ductility of the PI matrix, which prevents large deformations to occur before fracture.

Attempts were made to compare experimental moduli to theoretical predictions, using the well-known model developed by Halpin-Tsai.[44,45] This model is based on the early works of Hermans and Hill[46] and assumes that matrix and filler are linear elastic, isotropic and that there is a perfect bonding between the components. Moreover, the filler has to be uniform in its aspect ratio and perfectly aligned with the applied load. The Halpin-Tsai model gives the modulus of the composite (E_c) as a function of the modulus of the matrix polymer, E_m, and of the filler particles, E_f, and also as a function of the aspect ratio by the inclusion of a shape factor. The

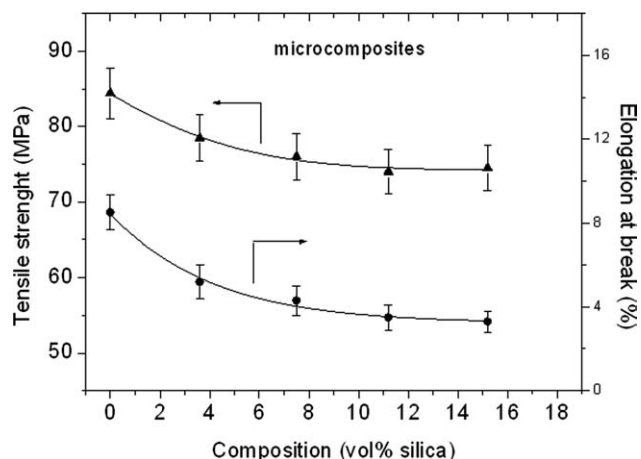
Figure 15 Elastic modulus for microcomposites (▲) and naocomposites (●) as a function of the silica content.

Figure 17 Tensile strength (▲) and elongation at break (●) for the microcomposite systems as a function of the silica content.
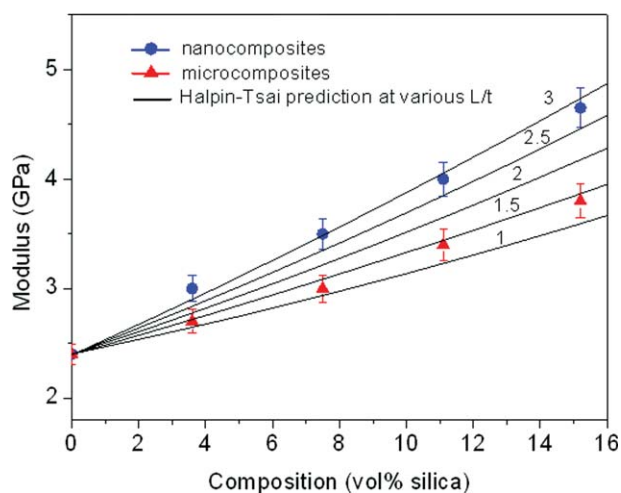
Figure 18 Elastic modulus as a function of silica content. Points are experimental data, and solid lines are the predication at various L/t using the Halpin-Tsai model. [Color figure can be viewed in the online issue, which is available at wileyonlinelibrary.com.]

predicted composite modulus is expressed in the form:

$$E_c = \frac{1 + \zeta \eta V_f}{1 - \eta V_f} E_m \qquad (3)$$

where ζ is a shape parameter dependent upon filler geometry and loading direction, V_f is the volume fraction of filler, and η is given by

$$\eta = \frac{E_f/E_m - 1}{E_f/E_m + \zeta} \qquad (4)$$

Halpin and Kardos[47] suggested that a shape factor of $\zeta = 2L/t$, where L is the length of the particle and t is its thickness, can be used for calculating the modulus of a polymer with the particles aligned along the loading direction.

The dependence of E_c, as predicted by eq. (3), on V_f, for different L/t values are shown in Figure 18, together with the experimental data. This figure shows that, for a fixed L/t, the predicted modulus increase almost linearly with increasing V_f and the efficiency in enhancing the stiffness increases with increasing L/t. From a comparison with the experimental data, one observe that for the microcomposites the modulus values are close to those predicted by the model with $L/t = 1.5$, whereas for the nanocomposites a good agreement is achieved for $L/t = 3.0$. For microcomposites, even if the adhesion between particles and matrix is relatively poor, the theory is still valid because the matrix-filler adhesion has a small effect on the modulus. Indeed, in the elastic case the degree of adhesion does not appear

to be an important factor as long as the frictional forces between the phases are not exceeded by the applied stress. Therefore, for microcomposites the reinforcement observed can be attributed principally to the shape of the silica particles and their unidirectional alignment along the applied stress, as showed by the SEM micrographs of Figure 6(a,b). These assumptions are consistent with numerous studies,[48–50] which proved that ellipsoidal or disc-shaped particles gave better reinforcement than spherical particles and that deviations from unidirectional alignment can result in reductions in composite stiffness. For the nanocomposites, the data of Figure 18 indicate that a good prediction is achieved when the aspect ratio is higher than that of spherical particles ($L/t = 1$) and that for $L/t = 1$ the prediction is quite poor. Considering that for nanocomposites, the silica nanoparticle are basically spherical, the poor agreement between the model with $L/t = 1$ and the experimental data may be due to the fact that the theory is very sensitive to filler aspect ratio but relatively insensitive to the large contribution arising from the high surface areas of silica nanoparticles. This feature leads to an enhancement in the interfacial modulus and consequently to composite moduli, which can be higher than those predicted by the theory.

Thermogravimetric analysis

In Figures 19 and 20 are shown the thermogravimetric (TG) curves, recorded in air at 10 °C/min, for the control PI and for hybrid composites loaded with various amounts of silica. For the pure PI, there is almost no weight loss before 450°C, but the degradation rate becomes very fast beyond that temperature, and almost all polymer chains are degraded abruptly
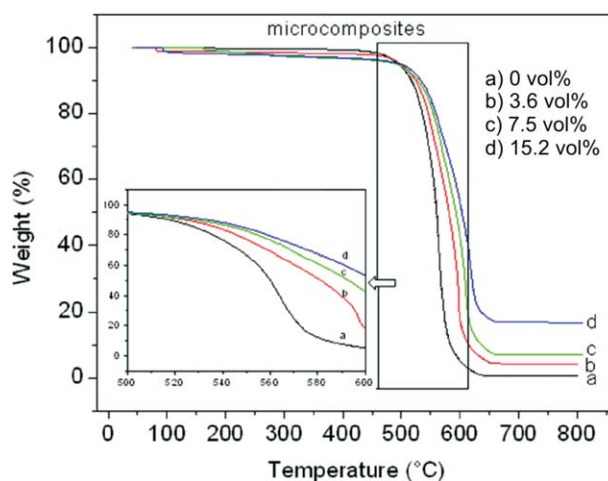

Figure 19 TGA curves for the pure polyimide and for microcomposite systems with various silica loadings. [Color figure can be viewed in the online issue, which is available at wileyonlinelibrary.com.]
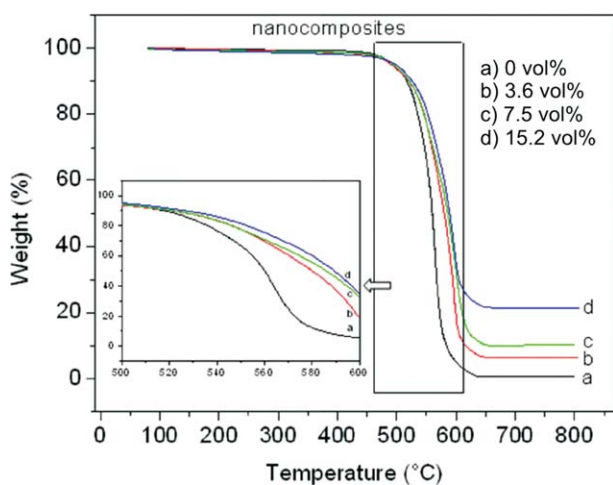
Figure 20 TGA curves for the pure polyimide and for nanocomposite systems with various silica loadings. [Color figure can be viewed in the online issue, which is available at wileyonlinelibrary.com.]

between 490 and 650°C. The presence of silica particles remarkably improves the thermal stability, shifting the TG curves to higher temperatures. The weight residue obtained after 700°C in the hybrids is quite proportional to the silica content, indicating that the sol–gel process was more or less complete.

In Table II are summarized the decomposition temperatures at which 5 wt % ($T_{0.05}$) and 50 wt % ($T_{0.5}$) weight loss occurred for the pure PI, nanocomposites, and microcomposites. The $T_{0.05}$ is a measure of the onset temperature of degradation, whereas $T_{0.5}$ is taken to be the midpoint of the degradation process. As can be seen, the values of $T_{0.05}$ for both hybrids increase slightly with increasing the silica content, while a marked enhancement in the $T_{0.5}$ values is observed as the silica concentration increases. This improvement is higher for microcomposites than for nanocomposites. For instance, at 15.2 vol % of silica $T_{0.5}$ increases of about 30°C for the nanocomposite and of about 38°C for the microcomposite. Generally, the improvement in the thermal stability of hybrid composites is related to the degree of the interaction between the polymer matrix and the inorganic phase and to the fact that the inorganic component has an inherently good thermal stability. Therefore, the lower thermal stability exhibited by the nanocomposites with respect to the microcomposites can be ascribed to the presence of the low molecular weight PI chains, deriving from the coupling agent, which reduce the hindering effect generated by the well-bonded silica nanoparticles to the degradation process. The aliphatic part of the aminosilane moiety may also play a role.

To better understand the effect of the silica phase on the thermal degradation behavior, TG measurements at various heating rates were also performed

and the results were subjected to thermal degradation kinetics studies.

For many kinetic processes, a rate of reaction, r, can be expressed as a product of the rate constant, k, and composition dependent term, $f(\alpha)$:

$$r = \frac{d\alpha}{dt} = kf(\alpha) \tag{5}$$

where α is the degree of conversion, defined as the ratio of the actual weight loss to total weight loss: $\alpha = m_0 - m/m_0 - m_\infty$, where m is the weight at time t (or at temperature T), m_0 is the initial weight, and m_∞ is the weight at the end of the experiment.

The rate constant, k, is a temperature dependent term that is assumed to follow an Arrhenius relationship:

$$k = A \exp\left(-\frac{E_d}{RT}\right) \tag{6}$$

where E_d is the degradation activation energy, and A is the pre-exponential factor.

In the case of polymer degradation, it is assumed that the rate of conversion is proportional to the concentration of material that has to react:

$$f(\alpha) = (1 - \alpha)^n \tag{7}$$

where n is the order of reaction. The combination of eqs. (4)–(6) gives the following relationship:

$$\frac{d\alpha}{dt} = A(1 - \alpha)^n \exp\left(-\frac{E_d}{RT}\right) \tag{8}$$

In this study two analytic methods: Ozawa[51,52] and Friedman[53,54] were used to analyze the thermogravimetric data.

The Ozawa method is based on the following equation:

$$\ln(\beta) = \ln[Af(\alpha)/(d\alpha/dT)] - E_d/RT \tag{9}$$

It assumes that the conversion function $f(\alpha)$ does not change with the heating rate for all values of α.

TABLE II
Temperature of Decomposition at 5 wt % ($T_{0.05}$) and at 50 wt % ($T_{0.5}$) Weight Loss for Polyimide and Hybrid Systems with Different Silica Amounts

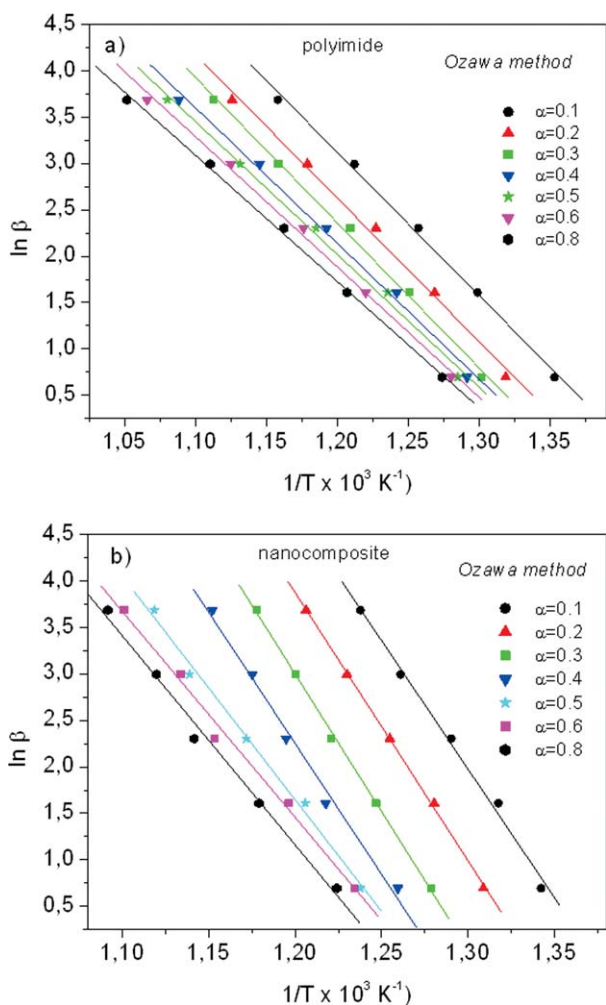| Silica (wt %)	Nanocomposites		Microcomposites	
	$T_{0.05}$ (°C)	$T_{0.5}$ (°C)	$T_{0.05}$ (°C)	$T_{0.5}$ (°C)
0	494.8	560.2	494.8	560.2
5	495.1	580.2	496.5	580.5
10	496.2	586.9	497.1	592.3
20	498.5	590.1	498.1	598.5

Figure 21 Typical Ozawa plots for the pure polyimide (a) and for a nanocomposite with 7.5 vol % of silica at different conversions (b). [Color figure can be viewed in the online issue, which is available at wileyonlinelibrary.com.]

The activation energy is evaluated by plotting ln β versus the reciprocal of temperature $(1/T)$ for a constant α; the slope of the line will be E_d/R. Some Ozawa plots are presented in Figure 21 for the pure PI [Fig. 21(a)] and for a nanocomposite with 7.5 vol % of silica [Fig. 21(b)]. An excellent linearity (correlation coefficients in the range 0.995–0.998) is obtained with all the evaluated conversion points (α = 0.1–0.8). However, for the pure PI the straight lines are nearly parallel, this being an indication that the activation energies at different degree of conversion are similar, whereas for the nanocomposite the straight lines are not parallel, suggesting a continuous change of degradation mechanisms. In Figure 22(a,b), the relationship between the activation energies and the degree of conversion for all the investigated systems are illustrated. The E_d for the neat PI can be considered to assume a constant average value that is reported in Table III. Conversely, for microcomposites and nanocomposites the depend-

ence of E_d on α is much greater and can be approximately separated in two distinct regions. The first for values of α up to 0.35, in which E_d can be considered as having a constant average value, and the second for α > 0.35 in which E_d shows a gradual decrease with increasing α. In this region, an average value for the activation energy was also estimated. In Table III, the averages of E_d calculated in both these regions are reported.

The Friedman method is based on the following equation derived from eq. (8):

$$\ln\left[\beta\left(\frac{d\alpha}{dT}\right)\right] = \ln A + n\ln(1-\alpha) - \frac{E_d}{RT} \quad (10)$$

The activation energy can be estimated by plotting $\ln[\beta(d\alpha/dT)]$ against $1/T$ for a constant α value. In analogy with the Ozawa method, if the kinetic does not change with the conversion, one should have a family of parallel lines having $-E_d/R$ as slope. The
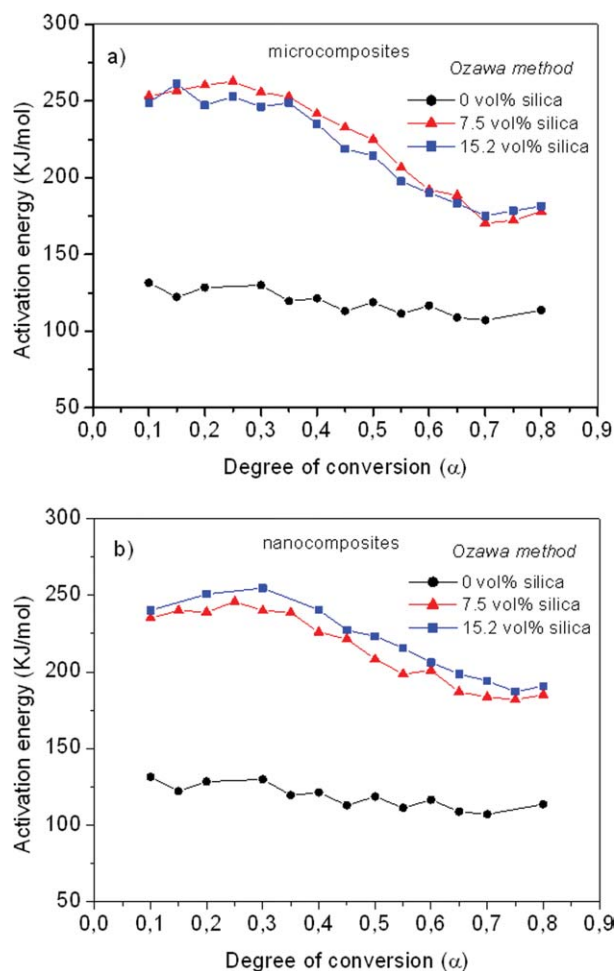

Figure 22 Dependence of activation energy on conversion as obtained by Ozawa method, for: (a) microcomposites with, 0, 7.5, and 15.2 vol % of silica; (b) nanocomposites with 0, 7.5, and 15.2 vol % of silica. [Color figure can be viewed in the online issue, which is available at wileyonlinelibrary.com.]

TABLE III
Activation Energy (E_d) for Polyimide and Hybrid Systems by the Ozawa Method

Silica (wt %)	Nanocomposites E_d (kJ/mol)	Microcomposites E_d (kJ/mol)
0	118.6	118.6
10	235.8 for α: 0.1–0.35	239.8 for α: 0.1–0.35
	198.7 for α: 0.4–0.8	199.3 for α: 0.4–0.8
20	242.6 for α: 0.1–0.35	246.5 for α: 0.1–0.35
	204.4 for α:0.4–0.8	205.3 for α: 0.4–0.8

TABLE IV
Activation Energy, E_d, for Polyimide, and Hybrid Systems by the Friedman Method

Silica (wt %)	Nanocomposites E_d (kJ/mol)	Microcomposites E_d (kJ/mol)
0	106.6	106.6
10	241.6 for α: 0.1–0.35	249.2 for α: 0.1–0.35
	202.2 for α: 0.4–0.8	197.1 for α: 0.4–0.8
20	239.5 for α: 0.1–0.35	248.6 for α: 0.1–0.35
	205.7 for α: 0.4–0.8	195.2 for α: 0.4–0.8

dependence of E_d on α for all the investigated systems, as obtained by the Friedman approach, is displayed in Figure 23(a,b). Similarly to the Ozawa method, the E_d for the pure PI does not vary substantially with α, whereas for the hybrid systems two values of E_d can be identified for the conversion intervals 0.1–0.35 and 0.4–0.8, respectively. The average E_d values obtained with the Friedman method are listed in Table IV.
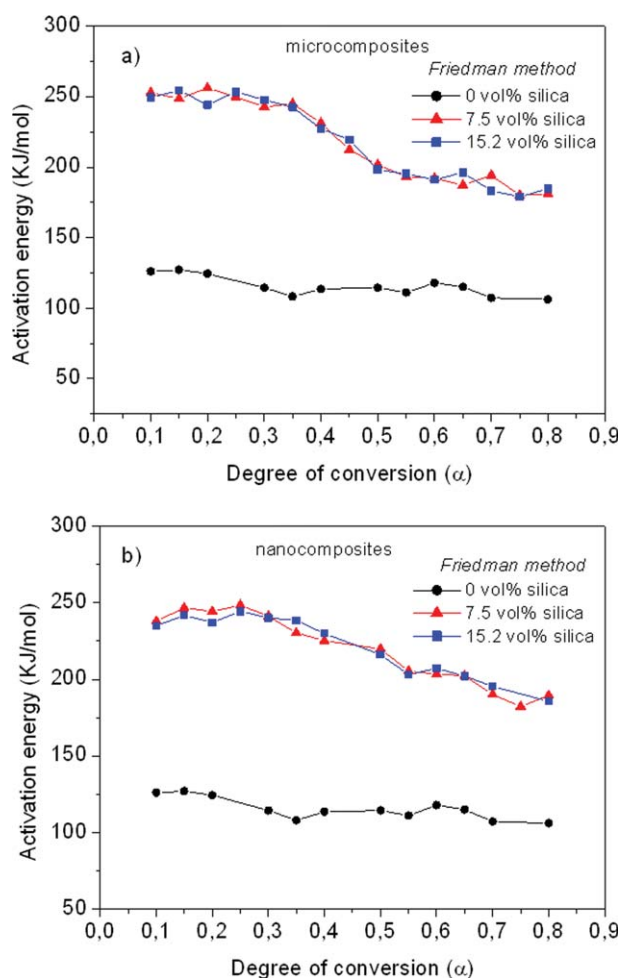

Figure 23 Dependence of activation energy on conversion as obtained by Friedman method, for: (a) microcomposites with, 0, 7.5, and 15.2 vol % of silica; (b) nanocomposites with 0, 7.5, and 15.2 vol % of silica. [Color figure can be viewed in the online issue, which is available at wileyonlinelibrary.com.]

From the whole of the kinetic data, it emerges that the activation energies computed by the two methods are very close to each other, thus confirming the reliability by analysis. Moreover, for microcomposites and nanocomposites there are no significant differences in the E_d values. However, the incorporation of silica particles produces a marked enhancement of activation energy. This effect may be the result of the thermal resistance of silica networks that not only, as reported previously, shifts the degradation of hybrids materials to higher temperatures but also promote their thermal stability presumably through the formation of a stable heat-resistant layer that may act both as a thermal insulator and as a barrier to oxygen diffusion in the bulk polymer.

The observed dependence of E_d on α for the hybrid materials also suggests that the inorganic phase changes the thermal degradation process with the occurrence of at least two different mechanisms. The first, with a higher E_d, is responsible for the early stages of the process with reduced mass loss, while the second, with lower E_d, represents the main decomposition mechanism, characterized by a substantial mass loss.

CONCLUSIONS

In this study, a fluorinated PI (6FDA-ODA) was synthesized and used as matrix for the preparation of PI/silica hybrids through the sol–gel process. The hybrids were characterized in terms of their molecular structure, morphology, viscoelastic behavior, thermal, and mechanical properties. The following conclusions were drawn:

- The compatibility between the PI and the silica phase was greatly improved by the use of an alkoxisilane-terminated oligoimide synthesized *ad hoc*. Microcomposites with silica particles having a smooth surface and scarcely bonded to the surrounding matrix were obtain in the absence of the coupling agent, while nanocomposites with silica domains well bonded to the PI matrix were achieved in the presence of the coupling agent.
- Dynamic viscoelastic measurements showed for both the types of hybrids an increase in the

storage modulus below and above the glass transition temperature. The nanocomposite hybrids exhibited superior T_g and T_β values, higher activation energy for the β transition, and a more efficiency in suppressing the α and β relaxation processes. All these effects were attributed to the highly interconnected silica domains, characterizing the morphology of nanocomposites, which restricted the segmental mobility of the PI chains involved in the visco-elastic losses.

- Mechanical studies showed enhanced moduli for both the microcomposite and the nanocomposite hybrids. This reinforcing effect was higher for the nanocomposites and was attributed to the better interfacial strength and reduction in sizes of the silica particles. The measured moduli were also compared with theoretical values, calculated using the Halpin–Tsai model. The tensile strength for microcomposites constantly decreased with increase in silica contents. A different trend was observed for nanocomposites for which the mechanical strength increased regularly up to a silica content of about 7.5 vol % and then it decreased slightly. This behavior was ascribed again to the morphology of the nanocomposites, which allowed more efficient stress-transfer mechanisms.

- TGA measurements revealed that thermal decomposition temperatures and degradation activation energy of the hybrid systems were much higher than that of the pure PI. These effects were attributed to the higher thermal stability of the silica phase and to the formation of a silica layer that shielded the polymer matrix from oxidative processes. According to the Ozawa and Friedman models of analysis, the thermal degradation of PI was found to be adequately represented by one mechanism, whereas for the hybrid materials at least two degradation mechanisms having different activation energies were operative.

References

1. Ghosh, M. K.; Mittal, K. L., Eds. Polyimide: Fundamentals and Applications; Marcel Dekker; New York, 1996.
2. Bessonov, M. I.; Zubkov, V. A. Polyamic Acids and Polyimides: Synthesis, Transformation and Structure; CRC Press: Boca Raton, F.L; 1993.
3. Thompson, L. F.; Wilson, C. G.; Tagawa, S., Eds. Polymers for Microelectronics: Resists and Dielectric. ACS symposium series, 537; ACS: Washington DC, 1994.
4. Yang, Y. K.; Koros, W. J.; Hopfenberg, H. B.; Stannet, V. T. J Appl Polym Sci 1986, 31, 1619.
5. Hofman, D.; Ulbrich, J.; Fritsch, D.; Paul, D. Polymer 1996, 37, 4773.
6. Morikawa, A.; Iyoku, Y.; Kakimoto, M.; Imal, Y. Polym J 1992, 24, 107.
7. Mascia, L. Trends Polym Sci 1995, 3, 61.
8. Ahmad, Z.; Mark, J. E. Chem Mater 2001, 13, 3320.
9. Ahmad, A. M.; Ahamad, Z. J Mater Sci 2007, 42, 8363.
10. Nandi, M.; Conklin, J. A.; Salvati, L.; Sen, A. Chem Mater 1991, 3, 201.
11. Huang, H.; Glaser, R. H.; Wilkes, G. L. In Inorganic and organo-matallic polymers; Zeldin, M.; Winne, K. J.; Allcock, H. R., Eds.; ACS symposium series, 360. ACS; Washington DC, 1987.
12. Wang, L.; Tian, Y.; Ding, H.; Li, J. Euro Polym J 2006, 42, 2921.
13. Brinker, C. J.; Scherer, G. W. Sol-Gel Science: The Physics and Chemistry of Sol-Gel Processing; Academic press; London, 1990.
14. Wang, S.; Ahmad, Z.; Mark, J. E. Chem Mater 1994, 6, 943.
15. Kioul, A.; Mascia, L. J Noncryst Solids 1994, 175, 169.
16. Iyoku, Y.; Kakimoto, M.; Imai, Y. High Perform Polym 1994, 6, 43.
17. Schrotter, J. C; Smaihi, M.; Guizard, C. J Appl Polym 1996, 6, 99.
18. Al-Kandary, S. H.; Ali, A. A. M.; Ahmad, Z. J Mater Sci 2006, 41, 2907.
19. Musto, P.; Ragosta, G.; Scarinzi, G.; Mascia, L. Polymer 2004, 45, 1697.
20. Ragosta, G.; Musto, P.; Abbate, M.; Russo, P.; Scarinzi, G. Macromol Symp 2007, 247, 88.
21. Musto, P.; Abbate, M.; Lavorgna, M.; Ragosta, G.; Scarinzi, G. Polymer 2006, 47, 6172.
22. Musto, P.; Ragosta, G.; Scarinzi, G.; Mascia, L. Polymer 2004, 45, 4265.
23. Musto, P.; Ragosta, G.; Mensitieri, G.; Lavorgna, M. Macromolecules 2007, 40, 9614.
24. Musto, P.; Mascia, L.; Mensitieri, G.; Ragosta, G. Polymer 2005, 46, 4492.
25. Wang, S.; Ahmad, Z.; Mark, J. E. J Macromol Sci Macromol Rep 1994, 31, 411.
26. Mark, J. E.; Wang, S.; Ahmad, Z. Macromol Symp 1995, 98, 731.
27. Huang, Y. Gu, Y. J Appl Polym Sci 2003, 88, 2210.
28. Saeed, S.; Khalil, M.; Ahmad, Z. J Macromol Sci Part A: Pure Appl Chem 2009, 46, 152.
29. Khalil, M.; Saeed, S.; Ahmad, Z. J Appl Polym Sci 2008, 107, 1257.
30. Chen, B.-K.; Chiu, T.-M.; Tsay, S.-J. J Appl Polym Sci 2004, 94, 382.
31. Hu, Q.; Marand, E.; Dhingra, S.; Fritsch, D.; Wen, J.; Wilkes, G. J Memb Sci 1997, 135, 65.
32. Joly, C.; Goizet, S.; Schrotter, J. C.; Sanchez, J.; Escoubes, M. J Memb Sci 1997, 130, 63.
33. Cornelius, C. J.; Marand, E. J Memb Sci 2002, 202, 97.
34. Yano, K.; Usuki, A.; Okada, A.; Kurauchi, T.; Kamigaito, O. J Polym Sci Polym Chem Ed 1993, 31, 2493.
35. Lan, T.; Kaviratna, P. D.; Pinnavaia, T. J Chem Mater 1994, 6, 573.
36. Wilson, D.; Stenzenberger, H. D.; Hergenrother, P. M., Eds. Polyimides; Blackie and Sons Limited: Glasgow, 1990.
37. Odian, G. Principles of Polymerization, 2nd ed.; John Wiley and Sons, New York, 1981.
38. Ishida, H.; Wellinghoff, S. T.; Baer, E.; Koening, J. K. Macromolecules 1980, 13, 826.
39. Parker, S. F. Spectrochim Acta A 2006, 63, 544.

40. Bellamy, L. J. The Infrared Spectra of Complex Molecules; Chapman and Hall: New York, 1975.
41. Colthup, N. B.; Daly, L. H.; Wiberley, S. E. Introduction to Infrared and Raman Spectroscopy; Academic Press: New York, 1990.
42. Qu, W.; Ko, T. M.; Vora, R. H.; Chung, T. S. Polymer 2001, 42, 6393.
43. Starkweather, H. W. J. Macromolecules 1990, 23, 328.
44. Halpin, J. C.; Pagano, N. J. J Compos Mater 1969, 3, 720.
45. Halpin, J. C. J Compos Mater 1969, 3, 732.
46. Hill, R. J Mech Phys Solids 1964, 12, 119.
47. Halpin, J. C.; Kardos, J. L. Polym Eng Sci 1976, 186, 344.
48. Bueche, A. M. J Polym Sci 1957, 25, 139.
49. Ahmed, S.; Jones, F. R. J Mater Sci 1990, 25, 4993.
50. Fornes, T. D.; Paul, D. R. Polymer 2003, 44, 4993.
51. Ozawa, T. Bull Chem Soc Jpn 1965, 38, 188.
52. Ozawa, T. J Therm Anal 1970, 2, 301.
53. Friedman, H. L. J Polym Sci Part C 1964, 6, 183.
54. Friedman, H. L. J Polym Lett 1966, 4, 323.